Blur remediation in NEAR MSI images

D. R. Golish[1], D. N. DellaGiustina[1], K. J. Becker[1], C. A. Bennett[1], M. Robinson[2], and M. K. Crombie[3]

[1]Lunar and Planetary Laboratory, University of Arizona, Tucson, AZ, USA

[2]School of Earth and Space Exploration, Arizona State University, Tempe, AZ, USA

[3]Indigo Information Services, LLC

Corresponding author:

Dathon R Golish (dgolish@orex.lpl.arizona.edu)

1415 N. 6th Ave. Tucson, AZ 85705

Keywords: Eros, Asteroids, Image processing

Abstract

Due to contamination on the outer optic of the NEAR-Shoemaker Multispectral Imager (MSI), all surface-resolved images of Eros acquired by MSI had wavelength-dependent degradation. The MSI team designed and implemented a preliminary correction for the blur during mission operations and archived the results with the original camera data. While extremely successful, the preliminary correction was less effective for the 450 and 1100 nm passbands. Here we implement a new correction, based on the MSI team's original process, to improve the blur remediation for all MSI filters, particularly those at the extreme wavelengths. The new method improves the effective resolution of the deblurred images over the preliminary remediation for all filters. Moreover, for all filters, our method preserves the 21-39% of the pixels that were lost (or obscured by artifacts) with the preliminary remediation. We apply the new method to the complete MSI dataset of resolved Eros images and archive the results for future scientific use.

1 INTRODUCTION

The Near Earth Asteroid Rendezvous – Shoemaker (NEAR; Cheng et al., 1997) spacecraft orbited and studied the surface of asteroid (433) Eros for a year from 14 February 2000 to 12 February 2001. Eros is a near-Earth S-type asteroid (Murchie, 1996); it is approximately 34 km long with an 11×11 km cross-section (Zuber et al., 2000). NEAR was the first mission to observe an asteroid from orbit and provided a broad dataset characterizing Eros's surface in unprecedented detail. Unfortunately, prior to these observations, during a failed orbit insertion maneuver on 20 December 1998, the NEAR thrusters expelled >28 kg of hydrazine fuel on to the spacecraft. Some fraction of this volume was deposited on to the outer optical surface of the NEAR Multispectral Imager (MSI; Hawkins, 1998; Murchie et al., 1999, 2002b), causing spectrally-dependent blurring for all of MSI's filters. The MSI camera was a five-element refractive telescope with eight filter positions. Seven narrowband filters covered wavelengths from 450 to 1050 nm, while one panchromatic filter covered from 600 to 800 nm. The blurring was worst at the shortest (450 nm) and longest (1050 nm) wavelengths. Because this contamination occurred before any surface-resolved imaging of Eros, the entirety of the resolved data set was degraded.

The MSI team took extensive observations of Canopus to characterize the point spread function (PSF) of the optics after contamination. These observations imaged Canopus in different regions of the detector and with all eight filters. Li et al. (2002) used a subset of these observations to develop a remediation and the NEAR team supplied those deblurred images to the Small Bodies Node (SBN) at the Planetary Data System (PDS).

Li et al. (2002) estimated a radially symmetric PSF for each MSI filter to deblur the images with a Fast Fourier Transform (FFT) based method. This method recovered much of the spatial resolution for the central wavelengths (550 – 1000 nm), though the extreme wavelengths were less successful (450, 1050 nm). In addition, limitations in the size of the FFT window led to cropping the image in one direction and strong artifacts on the edges of the images. The effective usable area of the restored images was therefore reduced (Li et al., 2002), however this shortcoming was mitigated by a targeting strategy that included extra overlap between images to ensure no coverage was lost. The remediation enabled all of NEAR's surface analysis and subsequent science. These analyses included global mapping (Buczkowski et al., 2008; Bussey et al., 2002; Veverka et al., 2000), color mapping (Murchie et al., 2002a; Riner et al., 2008), shape model and topographic analysis (Buczkowski et al., 2008; Thomas et al., 2002), geology (Cheng et al., 2002; Dombard et al., 2010; Izenberg et al., 2003; Robinson et al., 2002; Thomas and Robinson, 2005), and photometric modeling (Li et al., 2004).

We have the opportunity now, 20 years after MSI observed the surface of Eros, to improve upon this preliminary remediation in a number of ways. Increased computational resources allow us to deviate from efficiency-based design choices such as FFT windows that are powers of two, eliminating cropping and edge artifacts. Moreover, we can take advantage of the full set of Canopus images to develop a more advanced PSF model for each filter, including breaking the assumption of radial symmetry. The extent of the Canopus dataset suggested we might explore the feasibility of PSF that varies across MSI's field of view, though that proved not to be viable. In this manuscript, we detail the advanced modeling and deblurring process that we applied to the entire MSI orbital dataset.

2 MSI PSF

2.1 Deblurring algorithm

Our deblurring methodology is derived from the method used in the preliminary MSI remediation (Li et al., 2002). In both works, the degraded image, $g(x,y)$, is expressed as the convolution of the original signal, $f(x,y)$, and a distorting function, $h(x,y)$, with some additive noise, k.

$$g(x, y) = f(x, y) * h(x, y) + k \tag{1}$$

If we assume we can model or estimate the distorting (blurring) function and noise level, we can utilize a Wiener deconvolution to restore the original image (Dhawan et al., 1985). Wiener deconvolution is a common restoration method in which we transform the components to Fourier space with an FFT, invert the blurring function, and transform back to physical space to restore the original image. In this work, we used a built-in MATLAB function, *deconvwnr*, to perform the Wiener deconvolution. To evaluate the efficacy of the MATLAB function, we re-implemented the preliminary MSI remediation in MATLAB without *deconvwnr*. We verified that the MATLAB implementation produced identical results to the original MSI remediation. We then compared the results of the *deconvwnr* algorithm with the re-implementation of the preliminary MSI remediation method and found that the former had qualitatively improved noise reduction (evaluated by visual inspection).

The mathematical basis for our new method is otherwise similar, with one important difference. The preliminary remediation cropped the degraded images to 412×512 (from 412×537). While this was necessary for their implementation, it removed 25 lines (columns) from the images. Moreover, the discontinuous boundaries at the edges of the images caused FFT ringing (Figure 1(b)). Li et al. (2002) estimated that the usable pixel area of their remediated images was reduced to ~21% for monochromatic analyses and ~39% for color analyses. To avoid this loss, we make two changes. First, we remove the requirement that we perform FFT operations with powers of two (e.g., 512×512), so we do not have to crop the image. Secondly, we apply a tapered symmetric padding to all edges of the images. That is, we expand the image by an arbitrary amount (e.g., 50 pixels) in each direction and reflect the image data across the boundary. We then taper the data in the padded region such that the signal approaches 0 at the new edges of the image (Figure 1(c)). This forces the image to be approximately zero at all boundaries and FFT artifacts that result from edge discontinuities are eliminated. Even without improved remediation (Section 3), these changes alone restore the lost pixels, increasing the usable areas by 21-39%.

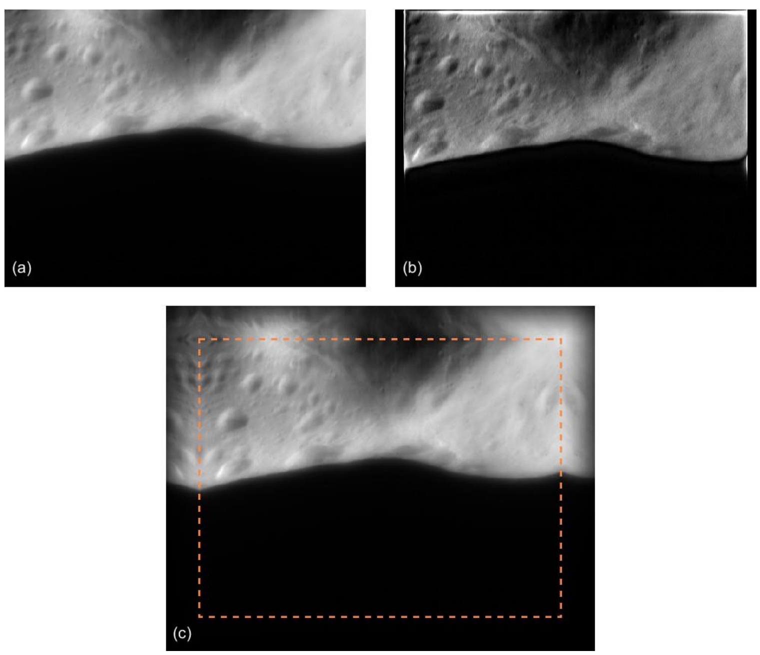

Figure 1: Correcting a degraded image (m0128004492, acquired at 09:31:06 on 2000 March 09, 14 km wide) with its original aspect ratio (a) will produce FFT artifacts at the edges (b). Applying a tapered symmetric padding (c) across this boundary (dashed orange line) eliminates the artifacts.

2.2 Point Source Data

To apply the remediation algorithm, we must estimate the distorting function (i.e., the system PSF after hydrazine decontamination, $h(x,y)$ in Eqn. 1). After the hydrazine contamination event, MSI collected >7,000 images of Canopus in all eight filters and in several regions of the detector. MSI acquired the Canopus images throughout 1999, 2000, and 2001, however the MSI team saw no evidence of temporal changes in the MSI PSF (Li et al., 2002) and our analysis confirmed this. The MSI team designed the Canopus observations such that Canopus fell in one of nine regions (in a 3x3 grid) of the detector. With the exception of the extreme wavelengths (450 and 1100 nm) and the panchromatic filter, MSI imaged Canopus in all nine regions for the five remaining filters. For those underrepresented filters, MSI imaged Canopus in regions 3, 5, and 8 (Figure 2). However, the majority of images for all filters were in the central region, even those with full coverage acquired as few as 16 images in each region, as shown in Table 1.

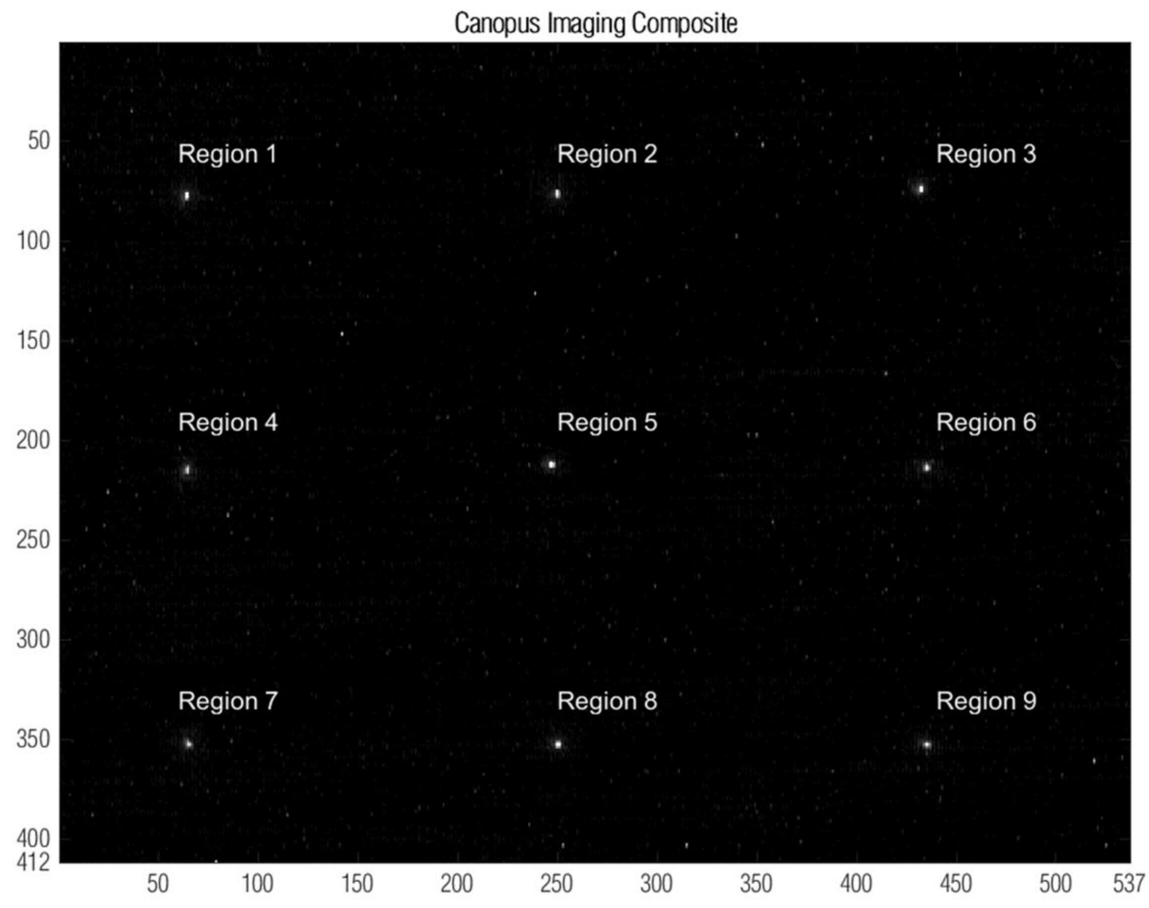

Figure 2: Composite of nine Canopus images with filter 4 (900 nm) in the nine detector regions.

Table 1: Region layout and number of images of Canopus acquired by MSI per region and filter acquired

Filter 1 (550 nm)		
16	16	32
16	667	16
16	94	16

Filter 2 (450 nm)		
0	0	16
0	642	0
0	88	0

Filter 3 (760 nm)		
16	12	32
16	659	16
16	107	16

Filter 4 (950 nm)		
16	16	32
16	804	16
16	93	16

Filter 5 (900 nm)		
16	16	32
16	599	16
16	65	16

Filter 6 (1000 nm)		
16	16	32
16	549	16
16	96	16

Filter 7 (1050 nm)		
0	0	16
0	1376	0
0	173	0

Filter 0 (pan)		
0	0	16
0	532	0
0	43	0

2.3 Aspect Correction

All Canopus images are available on the PDS SBN in the Eros MSI Cruise and Orbit bundles. The MSI team archived all MSI images in Flexible Image Transport System (FITS) format, with associated PDS3-style label files (per image) containing additional metadata. This work, for both PSF modeling and deblurring, uses the Level 2 calibrated MSI data archived with the SBN. Level 2 images are calibrated for bias signal, dark current, charge smear, responsive non-uniformity, and radiometric conversion (Murchie et al., 2002b, 1999).

The images were originally archived in their native pixel format – 244 rows by 537 columns, where the pixels are 27 × 16 μm. All data processed in this work and displayed in this manuscript have been aspect-corrected to 412×537 to accommodate the rectangular pixels. The resized images represent a physically meaningful aspect ratio. While we did explore modeling and correcting the image degradation in the native pixel space, as proposed by Li et al. (2002), we found that it did not fundamentally improve the remediation.

Our remediation, therefore, inherently included resizing the image. We resized the images with MATLAB's *imresize* function and a bicubic interpolator, though other interpolators (or resizing as part of the Fourier space remediation) are equally valid. Rather than embed another resizing process into the data, we elected not to compress the images back to their native pixel format after remediation. Any subsequent scientific analyses using MSI data will undoubtedly occur with aspect-corrected images. While this necessarily requires ~40% more storage space for the data, it avoids burdening the data with an additional noisy step that will be immediately reversed by any future users.

2.4 Reducing Data

Unfortunately, modeling of the MSI PSF is challenging owing to the presence of *aliasing* on the detector. The MSI detector was a frame transfer charge coupled device (CCD). Like many such devices (Golish et al., 2020; Sierks et al., 2011), the MSI pixels do not have 100% fill factor (Murchie et al., 1999). Anti-blooming channels between pairs of pixel columns obscured 8 μm bands (4 μm from each column) in an asymmetric pattern. An additional ~6.5 μm at the bottom of each pixel were not sensitive to light. As a result, the effective fill factor of the pixels was 0.5675, with aliasing in both the row and column directions. For an extended source, the insensitive regions blocked ~44% of the incoming light, but was accommodated by the radiometric calibration of the camera (Murchie et al., 2002b, 1999). However, when observing a point source, and with a PSF width on the order of a pixel, the fraction of the incoming light that was detected depended strongly on where the point source was imaged relative to the pixel grid.

Without exact point source locations, and a precise measure of the pixel geometry, automatic correction of the Canopus images is impossible. Instead, we coadded many images of Canopus such that we successfully sampled the peak of the PSF, while also increasing the signal to noise ratio (SNR) in the distal parts of the PSF, which are broad and dim.

To reliably combine 10s (or 100s) of point source images, we first had to center the images of Canopus for each filter/region combination. The pointing for every MSI image is described by the SPICE kernels archived by the Navigation and Ancillary Information Facility (NAIF; Acton et al., 2018). The SPICE toolkit allows us to calculate the right ascension and declination (RA/dec) for the four corners of a given image. We then transformed the nominal RA/dec (95.988° / -52.696°) of Canopus into an approximate pixel location for Canopus in the image. We cropped the image to an N x N window around the nominal Canopus location. The size of N depended on the filter, due to variation in the PSF width as a function of wavelength – 40 pixels for filters 0, 1, 2, and 3; 20 pixels for filter 5, 16 pixels for filters 4 and 6; and 10 pixels for filter 7. We calculated the weighted centroid of the resulting crop to identify the center of the image of Canopus. This method, which is highly sensitive to the broad, shallow wings of the PSF, consistently aligned the images. Optimizing the crop window was critical for this method. Too large a window allowed background noise and/or cosmic rays to perturb the weighted centroid. Alternatively, too small a window excluded the wings of the PSF and reduced the centroid fidelity.

For each filter/region combination, we then combined all available images of Canopus into a single image via a median operation. Because of aliasing on the detector, the central peak of a point source image could be masked by as much as 80% (Murchie et al., 1999). This had a negligible effect on the wings of the PSF – it consistently masked ~44% of the light, but was not dependent on the location of the PSF with respect to the pixel grid. The original remediation mitigated this effect by constructing a composite PSF from four concentric zones (Li et al., 2002). We mimic and simplify this mitigation by representing the PSF as the composite of two regions when combining Canopus images. For the central 3x3 pixel region surrounding the peak of the PSF, we included only the brightest images. This effectively assumed that for many locations of Canopus, with respect to the pixel grid, some fraction would be centered on the light-sensitive region. Setting this threshold too high would allow too many images where the PSF was not well centered. Setting it too low would reduce the SNR we gain by combining multiple images. We found that a threshold of 5% achieved an optimal balance between these two factors. However, for the underrepresented filter/region combinations, 5% of 16-32 images is only 1-2 images, which do not produce a meaningful median. Therefore, for those underrepresented regions, we also implemented a minimum, where at least three images must be included in every median. Again, this was a balance between too few and too many images. Clearly, the limited number of Canopus images outside of the central detector region reduced the statistical strength of this method.

Finally, we note that some MSI images had residual background noise (Figure 3). We expect that this noise, based on its sinusoidal structure, is likely uncorrected read noise from the detector electronics (Janesick, 2001). Moreover, the noise pattern is not eliminated by the median combination of several images, indicating that it is a somewhat fixed pattern in the detector readout. The level of the noise is sufficiently low (<4% of the peak signal) that it has negligible impact on any radiometric or morphological use of the images. However, for blur remediation, which includes modeling the wings of the PSF, a sinusoidal background can significantly perturb the model. Modeling of the noise proved ineffective – as likely to introduce artifacts as it was to remove the sinusoidal noise. Presumably, this noise source is best removed during image calibration. However, rather than attempt to recreate the MSI calibration pipeline, we instead simply set all negative pixel values in the co-added image to zero. This removed the majority of the sinusoidal pattern, but has no significant effect on our measurement of the PSF, which necessarily includes only positive values.

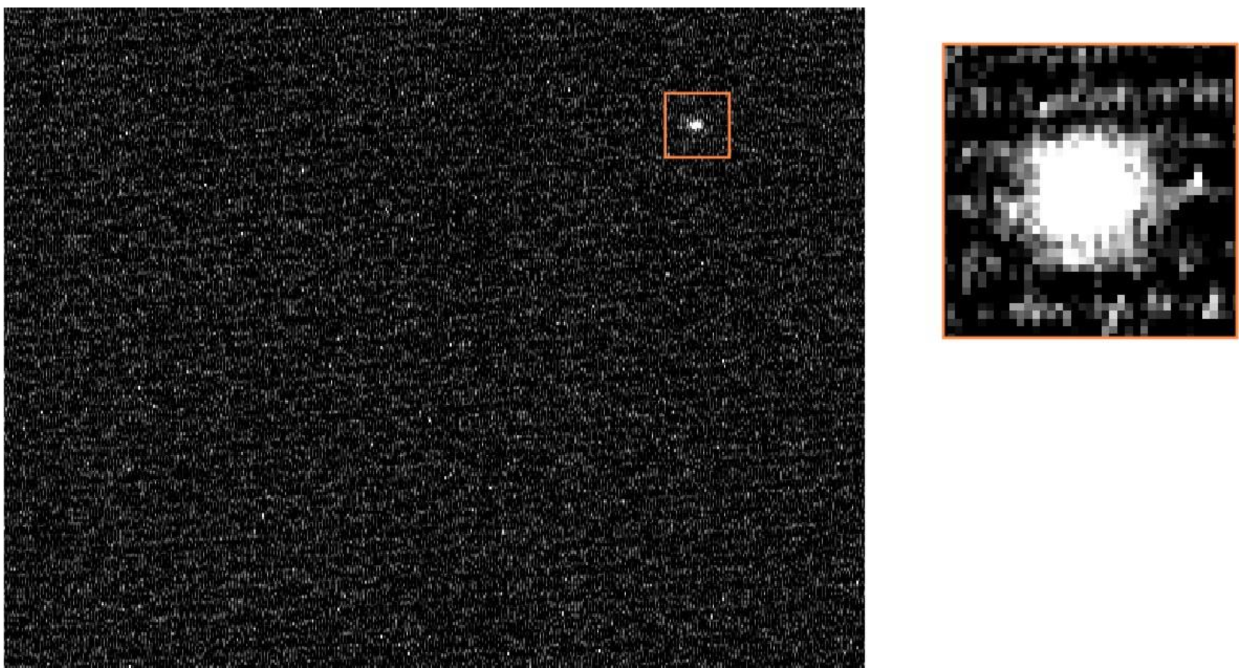

Figure 3: Sinusoidal background noise in the images can perturb the PSF model. Setting all negative pixel values to 0 removes the sinusoidal noise without significantly affecting the PSF measurement.

2.5 PSF Model

The original remediation represented the MSI PSF as a radially symmetric distribution, created by taking the median of many images of Canopus (utilizing the composite structure described in Section 2.4) and averaging the result in the radial dimension to increase the SNR (Li et al., 2002). In contrast, we modeled the MSI PSF functionally and not as the direct reduction of image data. The data averaging method used by Li et al. (2002) has the advantage that it can represent small variations in the PSF which a functional model is less likely to capture. This is particularly relevant for a PSF model, which is classically represented as a sinc function, which includes non-monotonic behavior in its wings. However, that representation is prone to variation due to noise. On the other hand, a functional representation has the advantage that it forces (with the appropriate functional form) physically realistic conditions (e.g., the PSF must always be positive). It is also more flexible, because we are able to create and adjust a PSF image (used in the deblurring process, Section 2.1) for any size array – as opposed to the data averaging method, which creates a fixed PSF image of a fixed size. This flexibility (particularly the ability to adjust the PSF on the fly) will be important for optimizing the PSF (Section 2.7).

The MSI PSF is characterized by a central peak, which broadened due to the contamination (Li et al., 2002), a relatively high shoulder, and broad shallow wings (Figure 4(a,d)). While the ideal representation of a PSF is a sinc function, the broad, shallow shoulder and wings cause a physically-motivated form to be insufficient. Instead, we chose to utilize an empirical form of the sum of three Gaussians. While clearly an approximation, the Gaussians allow us to capture the three components of the PSF (peak, shoulder, and wings) separately (Figure 4(b,e)). Moreover, the PSF is somewhat asymmetric; the three Gaussian form allows us to model the x (sample) and y (line) directions. The three Gaussian model has the form

$$I_{\mathrm{PSF}} = C_1 e^{-\left((x-x_1)^2/\sigma_{x1}^2 + (y-y_1)^2/\sigma_{y1}^2\right)} + C_2 e^{-\left((x-x_2)^2/\sigma_{x2}^2 + (y-y_2)^2/\sigma_{y2}^2\right)} + C_3 e^{-\left((x-x_3)^2/\sigma_{x3}^2 + (y-y_3)^2/\sigma_{y3}^2\right)} \quad (2)$$

where C_n is the peak value, σ_{xn} and σ_{yn} are the widths, and x_n and y_n are the center offsets, in the *x* (sample) and *y* (line) directions. We model the PSFs in MATLAB with the curve fitting toolbox (*fit*), using a non-linear least squares solver. The solver optimized the free parameters to minimize the difference between the measured data and the model. After fitting, the model is normalized and centered such that the peak of the model is equal to 1 and located at 0,0.

When compared with the PSF designed for the original remediation of 950 nm images (Figure 4(c,f)), the new remediation has a broader PSF, relative to its peak. The original remediation used the brightest pixel in any Canopus image to define the brightness of the central pixel of the PSF. This will inherently be larger than our method, which takes the median of the brightest 5% of the images for the central 3x3 pixel region. The PSF models for the original remediation were archived (and applied) as 512x512 FITS images. Correspondingly, there is some visible quantization in the original PSF model.

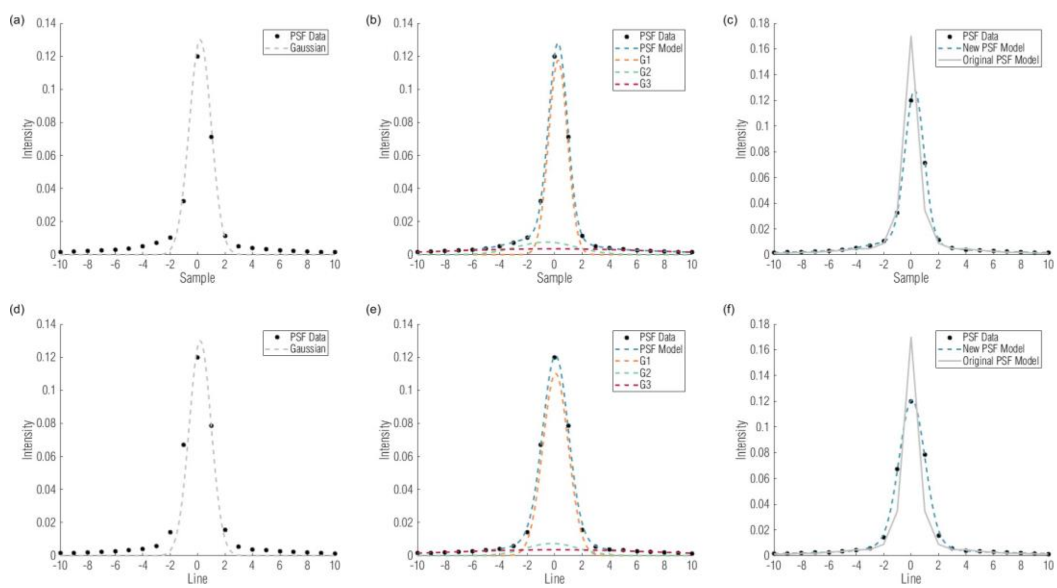

Figure 4: Modeling the 950 nm MSI PSF in the x/sample (a,b,c) and y/line(d,e,f) directions with a single Gaussian does not capture its width (a,d). Modeling it as the sum of three Gaussians captures the central peak, shoulder and wings (b,d). Compared with the PSF from the original remediation (c,f), we see a somewhat broader PSFs relative to its peak.

2.6 Spatial Variance

With more images in use than with the original remediation, we investigated whether a spatially variant PSF might improve the deblurring results. We repeated the analysis described above and produced PSF models for every region that has Canopus data. Unfortunately, the sparsity of data in the outer regions of the detector (Table 1) resulted in significant variation between the regions. Figure 5 shows cross-sections of the coadded Canopus images described in Section 2.4 for filter 4 (950 nm). Even for filter 4, which has the most post-contamination Canopus data, the peak value of the PSF varies by ~15% between regions. While the variation might be indicative of a spatially variant optical sensitivity, this is both physically unlikely (the contamination is on the outer surface of the lens only, not near any optical pupil) and unsupported by the data. All filters with Canopus data in more than three regions have region-to-region variability >12%. Filters 2, 7, and 0 only have Canopus imaging in three regions, making any spatial variation impossible to detect. Instead, we suspect that aliasing, which reduces the fidelity of the PSF measurement, results in apparent variation between the regions, some of which have only 16 or 32 measurements per filter (Table 1). Nonetheless, we did attempt to apply the PSFs modeled in the outer regions to evaluate their efficacy. In every case, a regional PSF recovered less image quality than the PSF designed from the center region, even in the area for which the regional PSF was designed. We conclude that there is not enough Canopus imaging in the exterior regions to support accurate PSF modeling, and by extension, a spatially variant correction. We elect to use only image data from the central region of each filter to model each per-filter PSF.

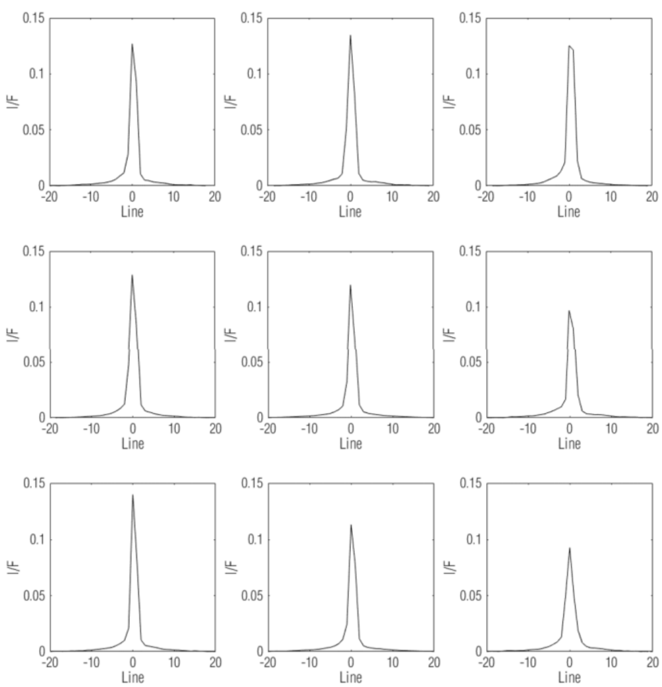

Figure 5: Cross-sections of coadded measurements of Canopus imaged with filter 4 (950 nm), shows significant variation between detector regions. Region layout matches that shown in Figure 2.

2.7 Manual PSF adjustment

Our initial application of the PSF models to deblur the image produced unsatisfactory results. Though the new PSFs recovered somewhat more information than the original remediation, they had a number of issues. Fortunately, the initial models were close and our functional modeling strategy allowed us to adjust the PSF and rerun the deblurring algorithm (Section 2.1) to mitigate these issues. We performed this process iteratively to optimize the PSFs.

The width of the central Gaussian in the PSF model was has the strongest influence on the amount of deblurring achieved. However, when deburring the original image (Figure 6(a)) with the automatically derived PSF model, the remediated images had columnar pixelization (Figure 6(b)). These artifacts are likely a result of the Fourier-based deblurring method (Section 2.1) and the high degree of aliasing on the MSI detector (Murchie et al., 1999). As discussed in Section 2.4, we selected a subset of Canopus images to model the central 3x3 region of the PSF to mitigate the impact of aliasing masking the true brightness of a point source. However, to the extent that this mitigation is imperfect, the PSF model for the central Gaussian will be less accurate. We found that narrowing the width of the central Gaussian in the *y* (line) direction helped reduce ringing around high contrast boundaries. Moreover, the MSI detector is asymmetrically aliased in *x* direction. Correspondingly, we found that increasing the width of the central Gaussian in the *x* (sample) direction reduced the columnar artifacts.

In practice, we found that the automatic model identified the width of the Gaussian representing the shoulder accurately. Small changes (~20%) in this width had little impact on the resulting deblurred images. However, our measurements of the wings of the models were noisy; the signal level in the wings is low and aliasing reduced the efficacy of the image coadding. The width of the Gaussian representing the wings controlled the extent to which the light spread, creating a ‘glow’ (Figure 6(c)) or ‘halo’ (Figure 6(d)) at transitions between a bright and dark area of the scene, e.g., the limb of the asteroid. As the width of the broadest Gaussian decreased, the glow on the limb increased. As the width increased, the halo surrounding the asteroid increased. We adjusted the width of the Gaussian to minimize the intensity of both effects, though the choice was inherently a trade-off between them.

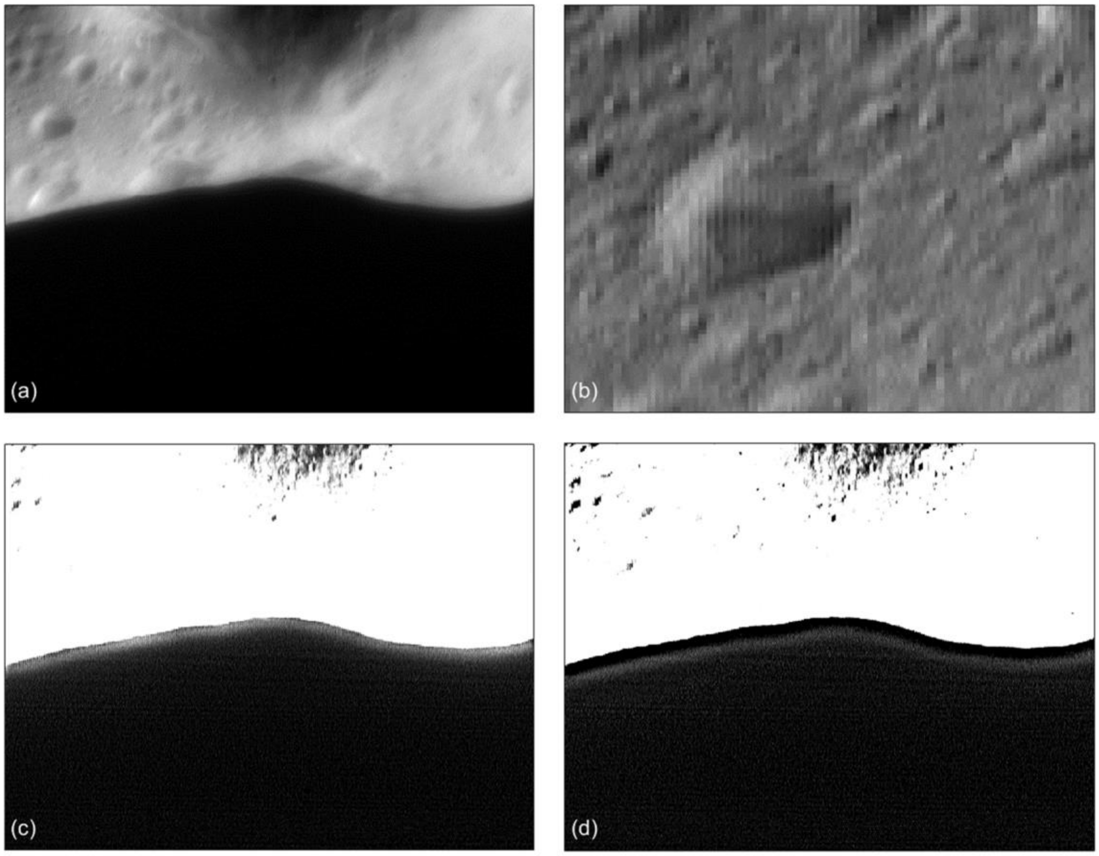

Figure 6: Recovering a contaminated MSI image (m012800492, a) with the automatically derived PSF model produced artifacts, including columnar noise (b), glow at high contrast boundaries (c), and halos at high contrast boundaries (d).

2.8 Determination of noise term

In the absence of noise, the ideal PSF would perfectly correct the degraded images. In practice, a variety of noise sources (e.g., read noise, shot noise, fixed pattern noise, stray light; (Janesick, 2001; Murchie et al., 2002b, 1999)) and an imperfect PSF model inhibit the correction by amplifying the noise. The noise term in a Wiener deconvolution (k in Eqn. 1) mitigates this effect by attenuating frequencies with low SNR. Practically, we must increase the noise term for images with lower SNR or when their PSF model is less accurate. Like Li et al. (2002), we find that a derived or automatically defined noise term does not perform well, so we define it by manually adjusting it to produce the best remediation. However, the noise term and PSF model are directly related. As such, determining the noise term is inherently a trade-off between improving image sharpness and amplifying noise and FFT artifacts.

We iteratively modified both the PSF shape and noise term to produce the best visual results. Unfortunately, we were not able to develop an automatic method of determining image quality. The artifacts introduced by over-processing the images have the same characteristics (e.g. high frequency content, high contrast, gradient steepness) that are typically used as image quality metrics. Therefore, we manually optimized the Gaussian width and noise terms to produce the best visual results (Table 2).

Table 2: PSF model parameters for each MSI filter

Filter (wavelength, nm)	**1 (550)**	**2 (450)**	**3 (760)**	**4 (950)**	**5 (900)**	**6 (1000)**	**7 (1050)**	**0 (pan)**
C_1	0.85	0.66	0.88	0.92	0.92	0.91	0.81	0.89
C_2	0.086	0.21	0.084	0.059	0.056	0.069	0.18	0.065
C_3	0.061	0.14	0.04	0.028	0.026	0.031	0.024	0.045
σ_{x1}	1.3	0.8	1.4	1.4	1.5	1.5	1	1.4
σ_{x2}	3.3	3	3	3	3.3	2.5	3	3.5
σ_{x3}	12	12	12	11	12	13	12	12
σ_{y1}	0.5	0.8	0.5	0.5	0.6	1	0.5	0.5
σ_{Y2}	3	3	3	3	2.8	2.5	3	3
$_{y3}$	12	12	12	11	12	11	12	12
x_1	0.0037	0.0061	0.0048	0.0055	0.0036	0.0081	0.0085	0.0032
x_2	-0.55	-0.16	-0.58	-0.86	-0.83	-0.79	-0.5	-0.53
x_3	-0.34	-0.31	-0.34	-0.41	-0.38	-0.33	-0.84	-0.23
y_1	0.00088	-0.0044	0.00095	0.0034	-0.0055	0.0085	0.0028	0.002
y_2	-0.021	0.067	-0.067	-0.25	0.4	-0.33	-0.041	-0.18
y_3	-0.078	-0.19	-0.061	-0.085	0.095	-0.022	-0.0076	-0.17
k	2	6	0.4	0.25	0.2	0.3	3	0.4

To determine these parameters, we performed a series of qualitative analyses. These analyses uses images that span the range of scenes imaged by MSI (e.g., whole disk, limb, well illuminated, and deeply shadowed).

We evaluate remediation images that include the limb (Figure 7(left)) by tracing profiles across the limb (Figure 7(right)), calculated as the median of several limb-crossing rows. Figure 7 illustrates the inherent trade-off: a sharper limb profile (lower *k*) indicates improved deblurring, but over-processing an image will lead to artifacts at the limb boundary. These artifacts manifest as ringing on either side of the discontinuity (most obvious in the top row), as well as a sharp peak and valley just before and after the limb. However, increasing the value of *k* to eliminate FFT artifacts (bottom row) results in poor deblurring performance and even that does not eliminate the peak before the limb. The valley after the limb is only eliminated because the limb has blurred enough to fill it in. Again, without a quantitative measure of accuracy, our parameters are guided by visual appearance and inherently qualitative. However, we make these choices informed by the needs of typical image data products (e.g., monochromatic maps and color ratios). We also evaluate images that don’t include limb by tracing profiles across high contrast features, such as high albedo features and deeply shadowed regions (Section 3.3). We evaluate examples such as these imaged with each filter to guide our selection of deblurring model parameters.

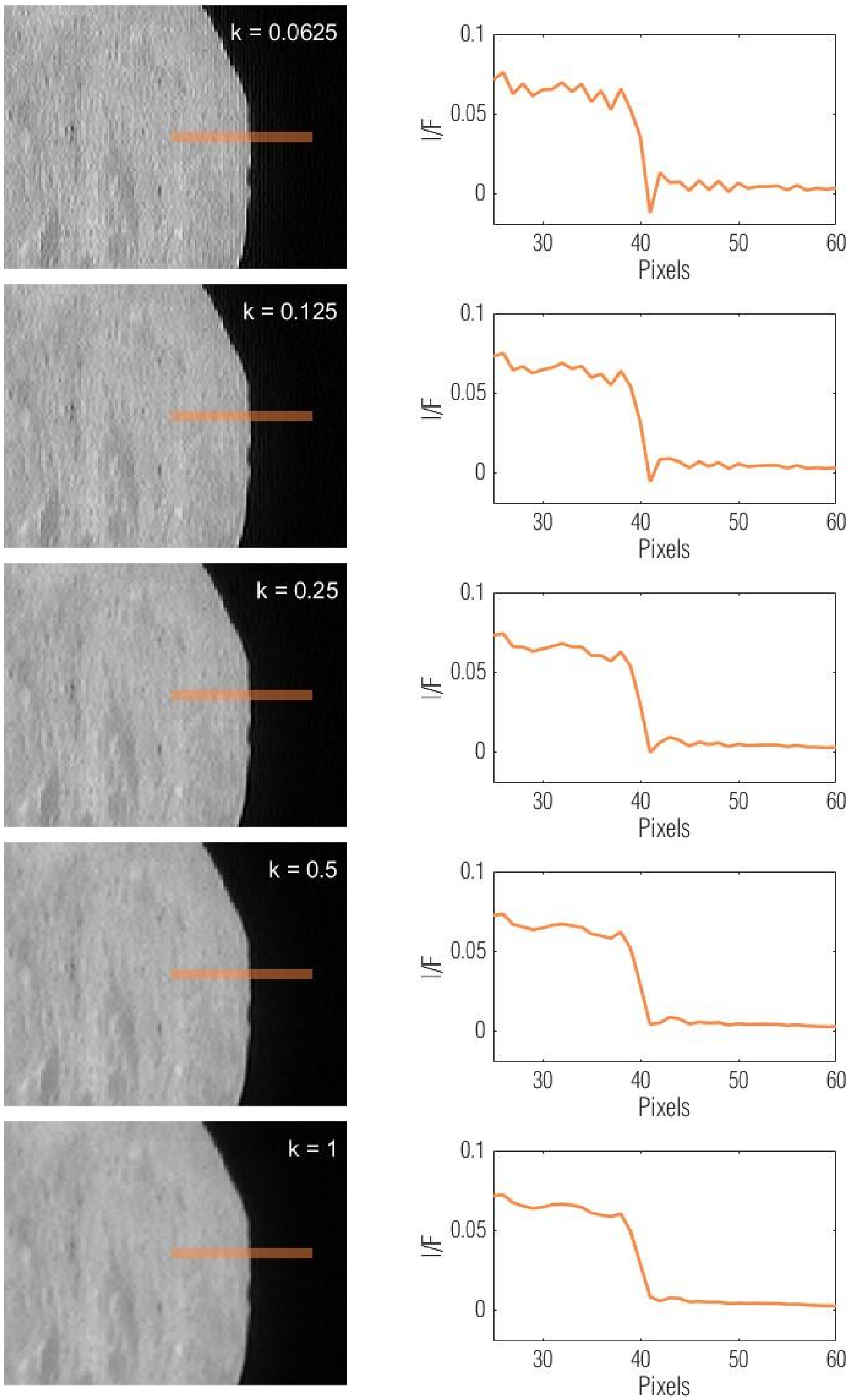

Figure 7: Limb profiles of a remediated image (m0151057156) help determine the design of the PSF and magnitude of the noise term. Setting the noise term low produces a sharp limb profile, but setting the noise term high reduces ringing around the limb.

3 REMEDIATION QUALITY

3.1 Qualitative summary

For all filters, the new remediation shows improvement over the preliminary version. We find that this is primarily due to an alternative PSF model that allowed us to reduce the noise term. The asymmetry of central Gaussian of the PSF model (σ_{x1} and σ_{y1} in Table 2) reduced the magnitude of FFT artifacts while improving image quality (Section 2.7), but the trade between sharpness and noise remains (Section 2.8). Though we evaluated the new remediation on a small subset of images (~100s out of the 100,000 image database), the improvement was consistent. This included for whole disk images (Figure 8(a,c,e)), limb images (Figure 8(b,d,f)), full field images (Figure 9), and images from every filter (Figure 10). The images shown in these figures are given identical grayscale stretches to highlight the improvement qualitatively. The depth of shadows (e.g., in craters) and reflectance on bright surfaces (e.g., crater rims) are enhanced in the new remediation, producing a sharper appearance. Moreover, FFT artifacts, visible extending ~10s of pixels from the edges of the images with the original remediation, are not present in the new remediation.

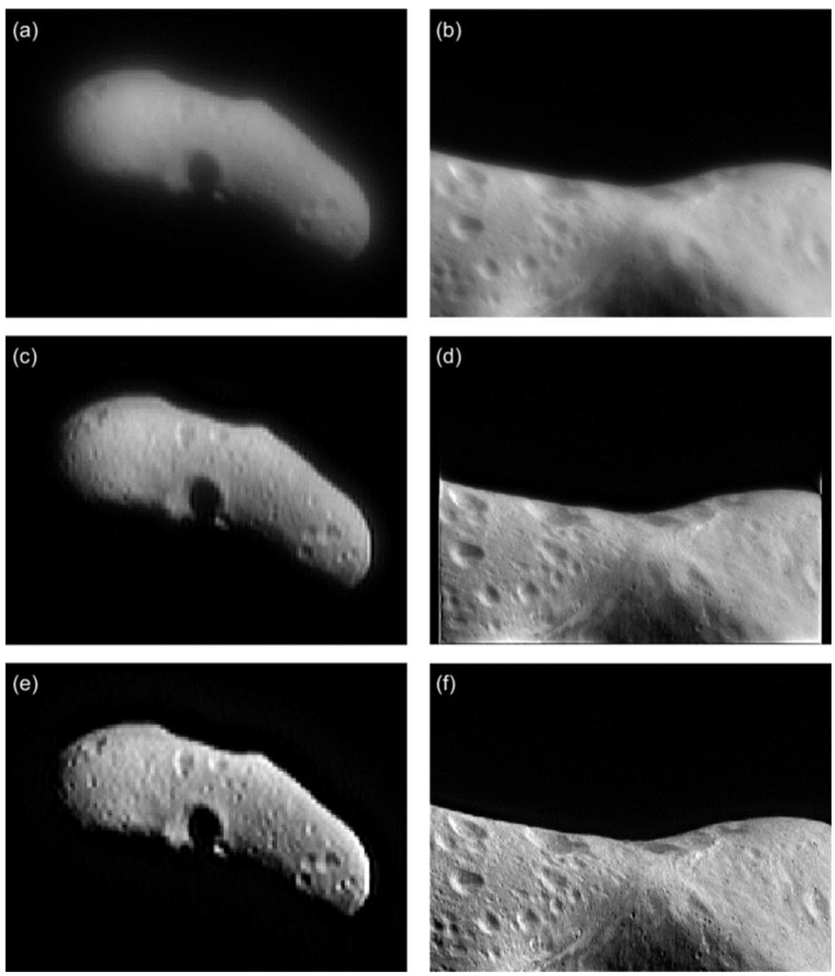

Figure 8: Degraded images m0125680533 (a) and m0128004492 (b) acquired with filter 4 (950 nm) improved significantly with the preliminary remediation (c,d; Li et al. 2002), but asymmetric PSF design allowed for further improvement in this work (e,f). Images on the left are cropped to a 165 x 127 window around the asteroid. An identical greyscale stretch is applied to each version of each image (different stretches for the two columns).

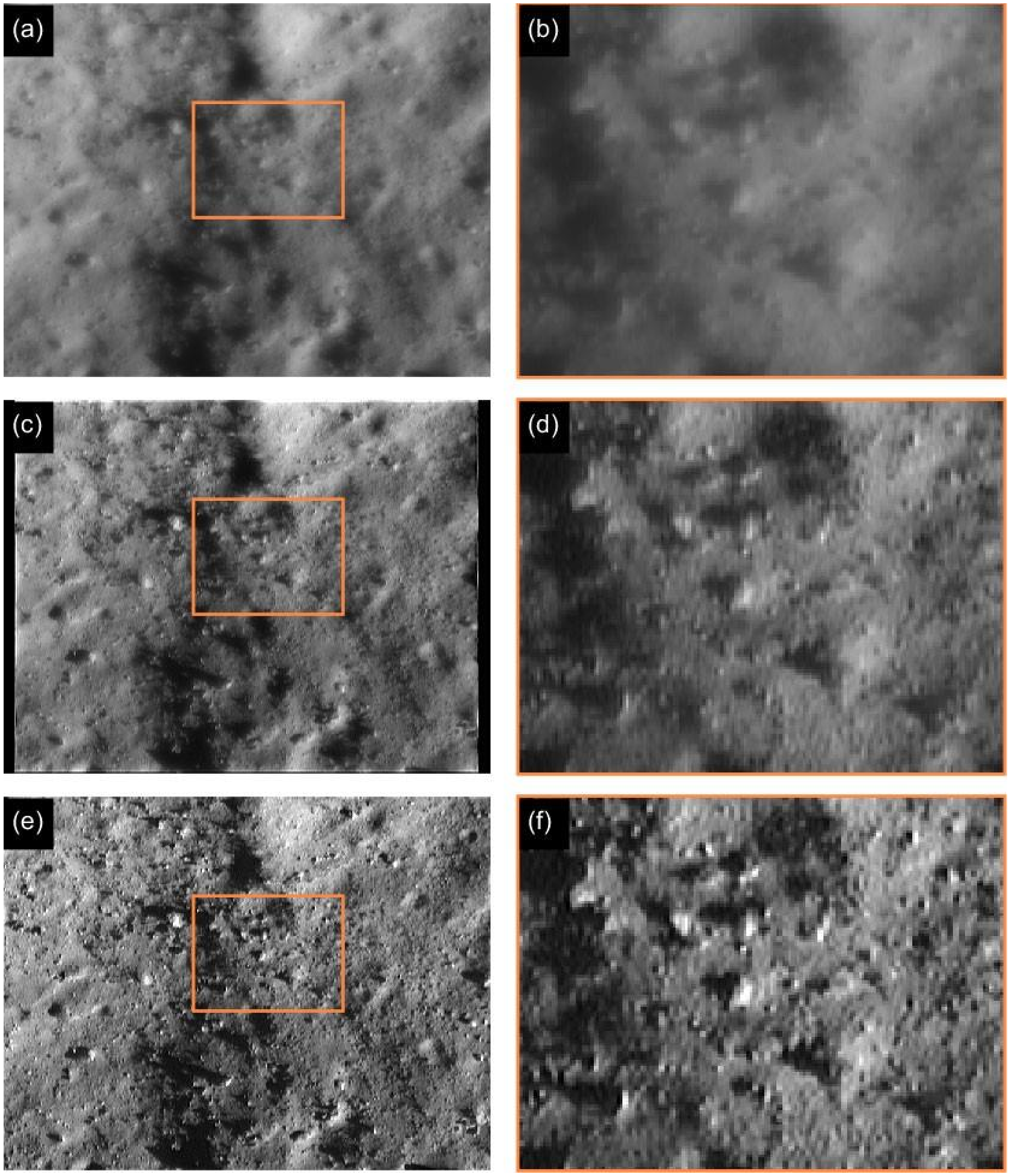

Figure 9: Additional example of degraded image m0153333885 (a,b) acquired with filter 4 (950 nm), its original remediation (c,d), and its new remediation (e,f). The right column (b,d,f) is a zoomed in region. All images have an identical grayscale stretch.

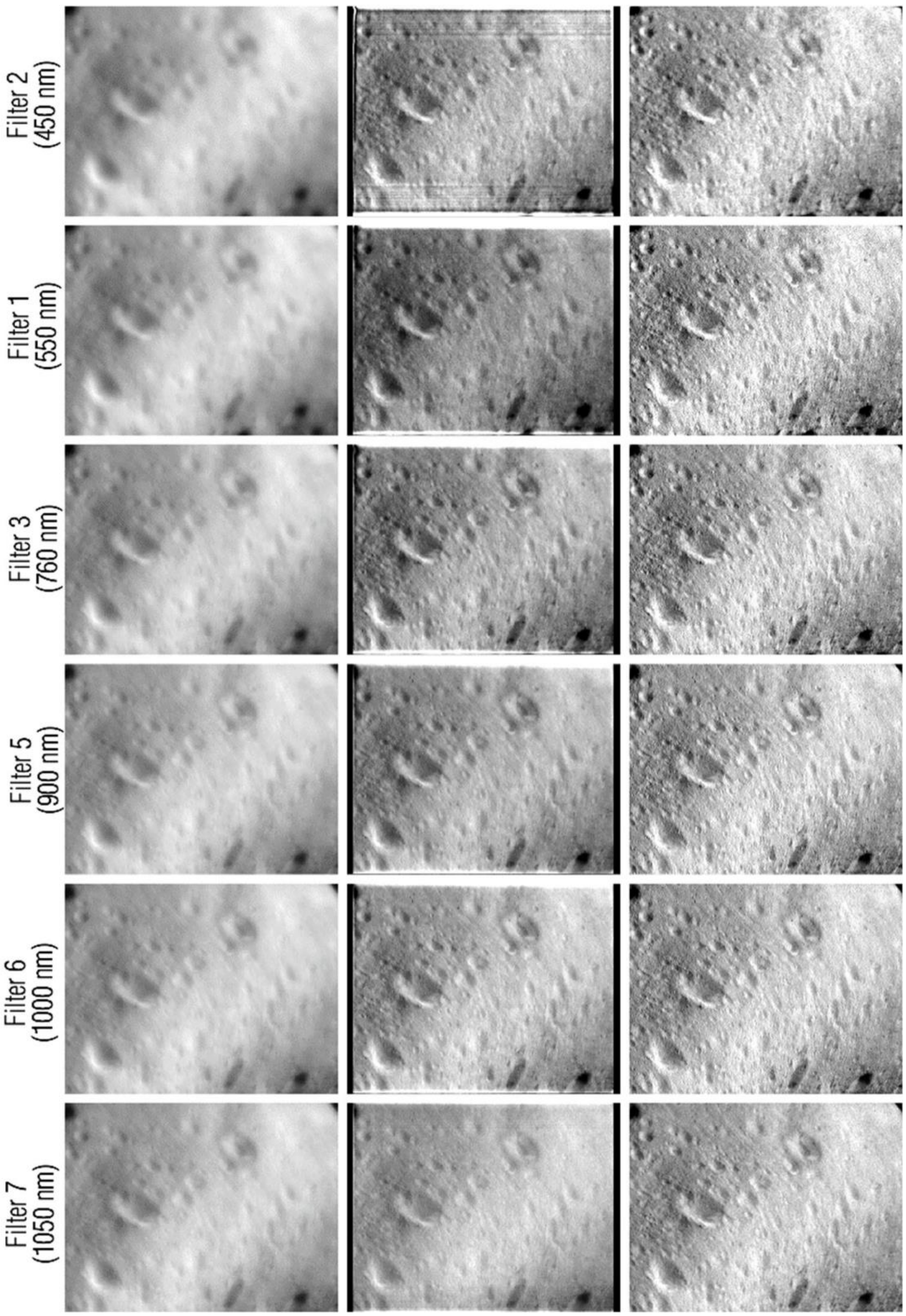

Figure 10: Degraded images (left), original remediation (middle), and new remediation (right) for additional filters. Image numbers are m0150981856, m0150981854, m0150981858, m0150981862, m0150981864, m0150981866 for filters 2, 1, 3, 5, 6, and 7, respectively. All three images from each filter have the same grayscale stretch.

3.2 Filters 2 and 7

As shown in Figure 10, all filters show improvement over the original remediation, but filters 2 (450 nm) and 7 (1050 nm) remain the least well corrected. As described in Li et al. (2002), the contamination had the largest impact on the extreme wavelength filters. In that original remediation, they were unable to correct these filters as well, and many had extreme FFT artifacts (Figure 10). As such, the PSF model we designed for these filters (Table 2), are noticeably different from the rest. Their central Gaussians are narrower with a smaller peak (relative to the other two Gaussian components). Moreover, the SNR of images acquired with these filters is uniformly lower than the other filters. The camera is less sensitive in filter 2 (450 nm) due to the quantum efficiency of the detector and transmission of the optics (Hawkins et al., 1997), necessitating exposure times 2.5-5X longer than the middle wavelengths. Exposure times are even longer (10-20X) for filter 7 (1050 nm), due to lower detector quantum efficiency at longer wavelengths (Hawkins et al., 1997). Using an unrealistically low noise term introduces speckle FFT artifacts (i.e., noise in the original image is amplified in the deconvolution process). As a result, we set the noise terms much higher in filters 2 and 7. This sacrifices some image quality, but avoids extreme FFT noise.

3.3 Quantitative analysis

We were not able to develop a thorough quantitative analysis of the improved remediation. As with identifying an 'ideal' noise factor (Section 2.8), such an analysis requires a robust quantitative quality metric. Every metric we investigated to design the deblurring parameters was sensitive to both image sharpness and high frequency noise. However, high-contrast surface features provide an opportunity to quantitatively evaluate the new remediation for particular geological units. Moreover, these are exactly the types of surface features that an improved remediation will allow further study of.

The geological features we analyzed included bright streaks (Selene crater at 760 nm; Figure 11), dark deposits (Psyche crater at 450 nm; Figure 12) and streaks (Psyche crater at 1000 nm; Figure 13), crater walls (Avtandil crater at 550 and Selene crater at 900 nm; Figure 14 and Figure 15), boulders (950 nm; Figure 16), and the asteroid limb (1050 nm; Figure 17). The analysis in these images traces a profile perpendicular to the contrast boundary created by the feature. We rotated the images such that the profiles were horizontal (i.e., along a row) and calculated the median of 5 rows around and including the profile line. The median partially smoothed the pixel-to-pixel variation that is present in the images, though an obvious residual variation remains in many examples and is discussed further below. The figures show an image corrected with the new and original remediations. The left column shows the full image; the middle column crops to the region of the profile. All images are given the same grayscale stretch. The absolute profiles (in units of I/F) are plotted in the top-right. Because the new remediation also includes new radiometric correction (Section 4), the mean I/F of an image can be different when compared with the original remediation. To remove this from the comparison, we calculate a linear fit to each profile and divide it into the profile. This effectively removes the absolute I/F calibration and any local reflectance slope. The result is shown in the middle-right plot for both methods and demonstrates how well the remediation methods resolve reflectance changes. Finally, the difference between these relative profiles is plotted in the bottom-right to provide a quantitative estimate of the remediation quality.

These examples provide a number of insights with respect to the quality of the new remediation. High contrast features are, in general, better resolved with the new remediation. That is, the contrast change ‘on’ and ‘off’ the feature is greater. This is illustrated by Figure 14, which traces a profile across the bright wall of Avtandil crater. The reflectance of the bright wall is 50% brighter than the surrounding terrain in the original remediation, but 65% brighter in the new remediation. Other examples of higher frequency features (such as bright and dark streaks), show similar behavior, but are muddled by high frequency noise. For example, the contrast variation between bright streaks in Selene crater (Figure 11) is amplified (i.e., the peaks and valleys are further from the reflectance average) in the new remediation, but noise in the image is similarly amplified. So while the bright streaks have ~5% higher contrast in the new remediation, background noise has ~2% higher contrast. This background noise is often visible in regions without measurable signal (such as deep shadows or off-limb), where scene-independent noise (e.g., shot noise, read noise, uncorrected dark current) is amplified. This reinforces the fundamental trade-off between sharpness and noise (Section 2.8). Often, as in the 450 nm image of dark deposits on Psyche crater (Figure 12), the noise is present in both methods, but the noise is better ‘resolved’ with the new remediation. Nonetheless, high contrast features, such as the transition between a boulder’s shadow and its sunlit side (Figure 16), show tens of percent increase in contrast with the new remediation. Limb profiles, which were partially used to design the new PSF and noise terms, show a similar level of improvement (Figure 17). These examples are a very small fraction of the large MSI Eros dataset and they have been chosen to highlight the improvement made possible by the new remediation. Many images have minimal improvement over the original remediation, though we have not found any that show degradation. Nonetheless, because the new images have generally improved sharpness, they often have generally increased noise.

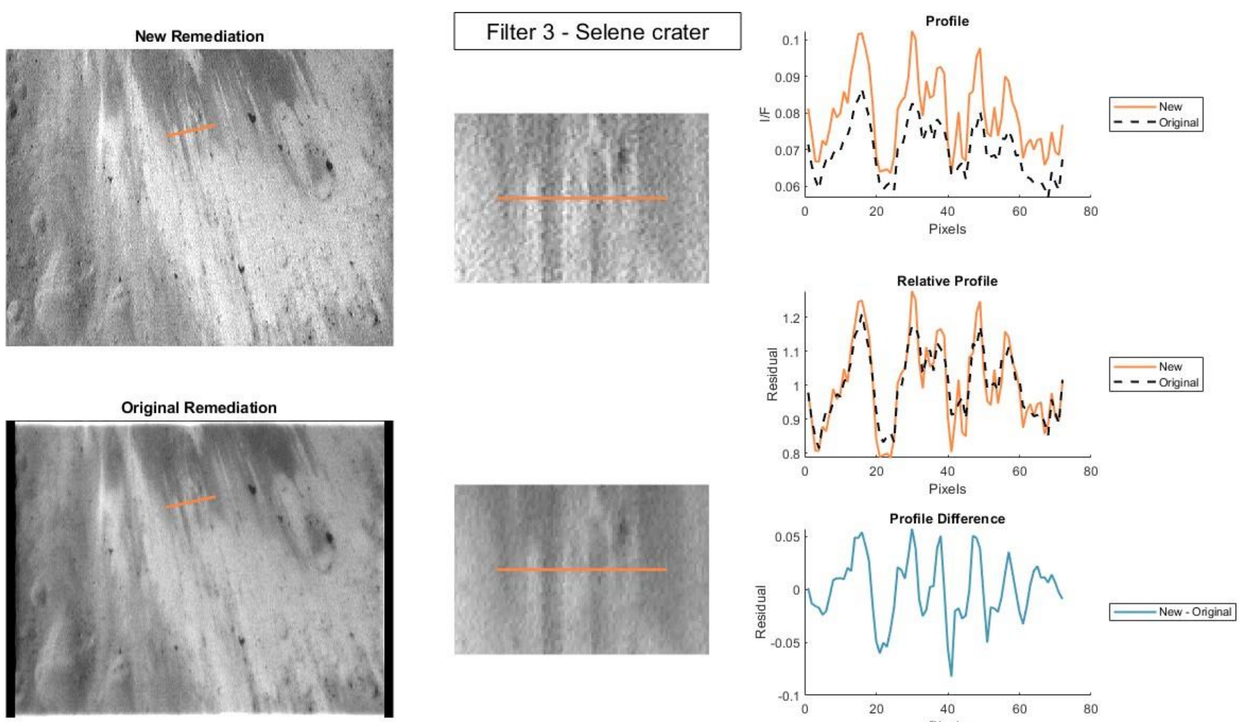

Figure 11: Profile analysis of bright streaks in Selene crater, imaged at 760 nm (m0155816391).

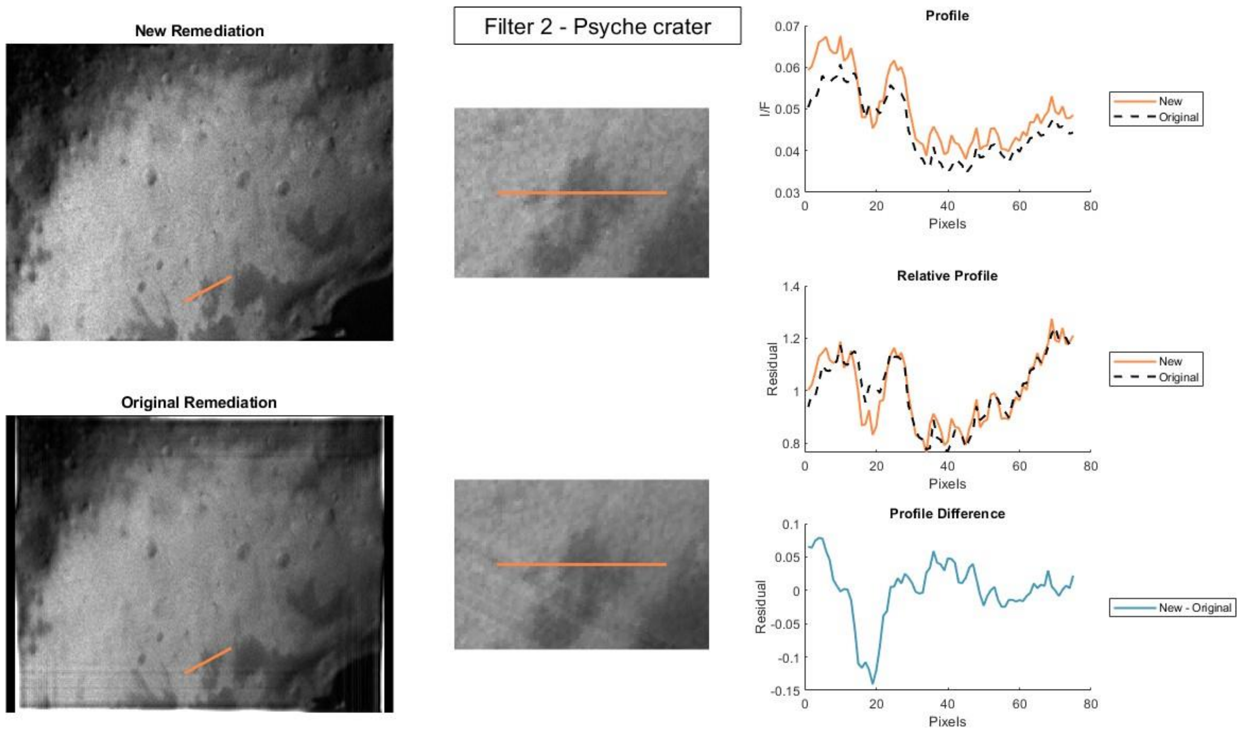

Figure 12: Profile analysis of dark deposits in Psyche crater, imaged at 450 nm (m0141515386).

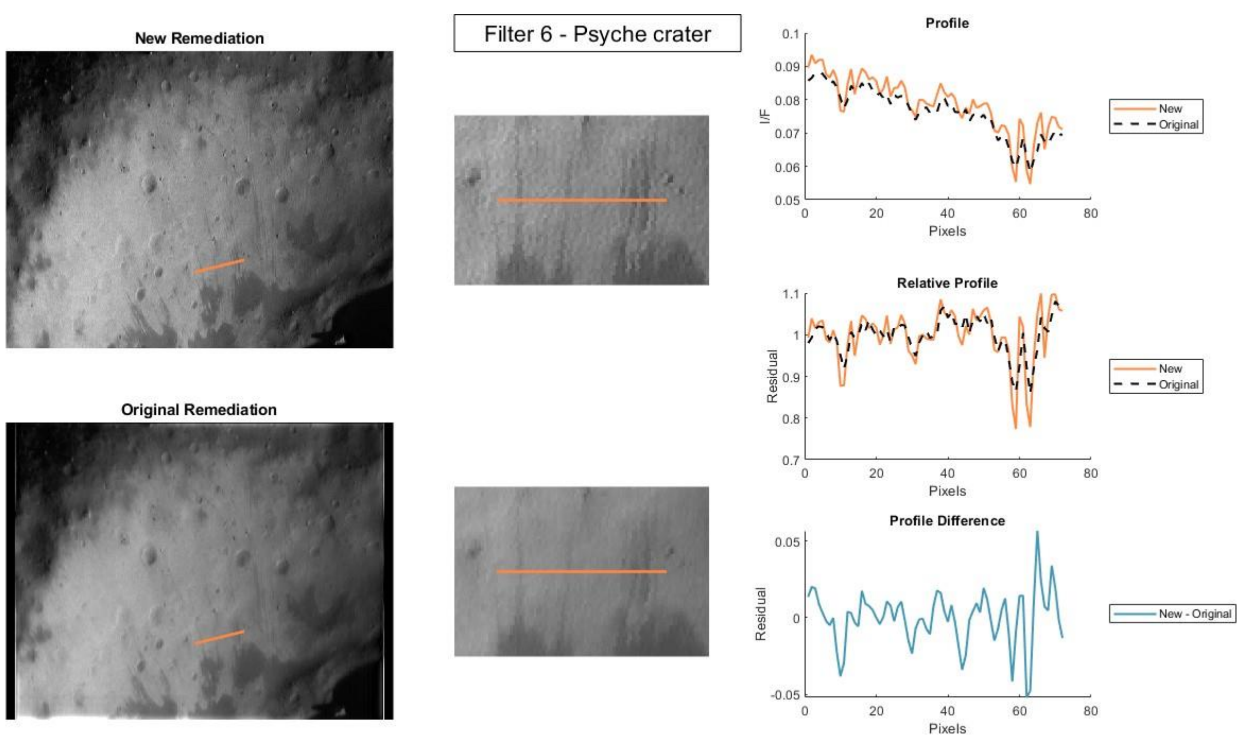

Figure 13: Profile analysis of dark streaks in Psyche crater, imaged at 1000 nm (m0141515392).

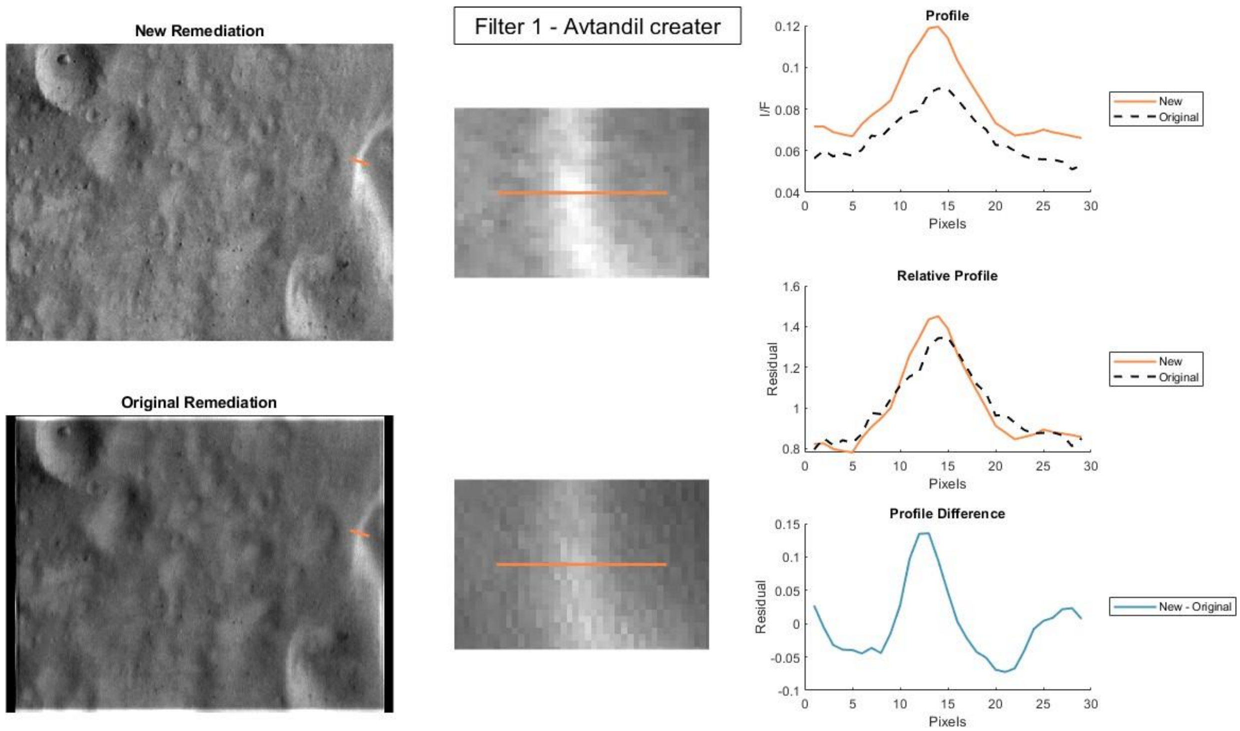

Figure 14: Profile analysis of a bright wall in Avtandil crater at 550 nm (m0155204785).

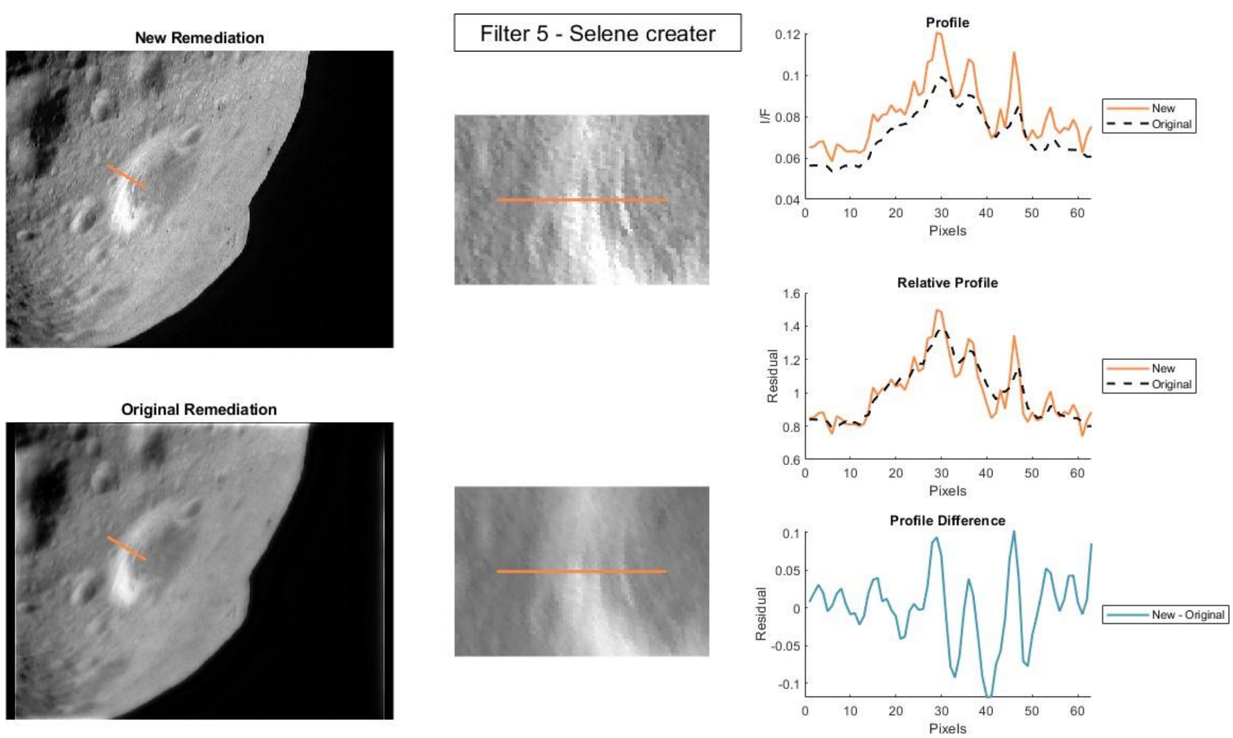

Figure 15: Profile analysis of an obliquely viewed crater wall in Selene crater at 900 nm (m0150009792).

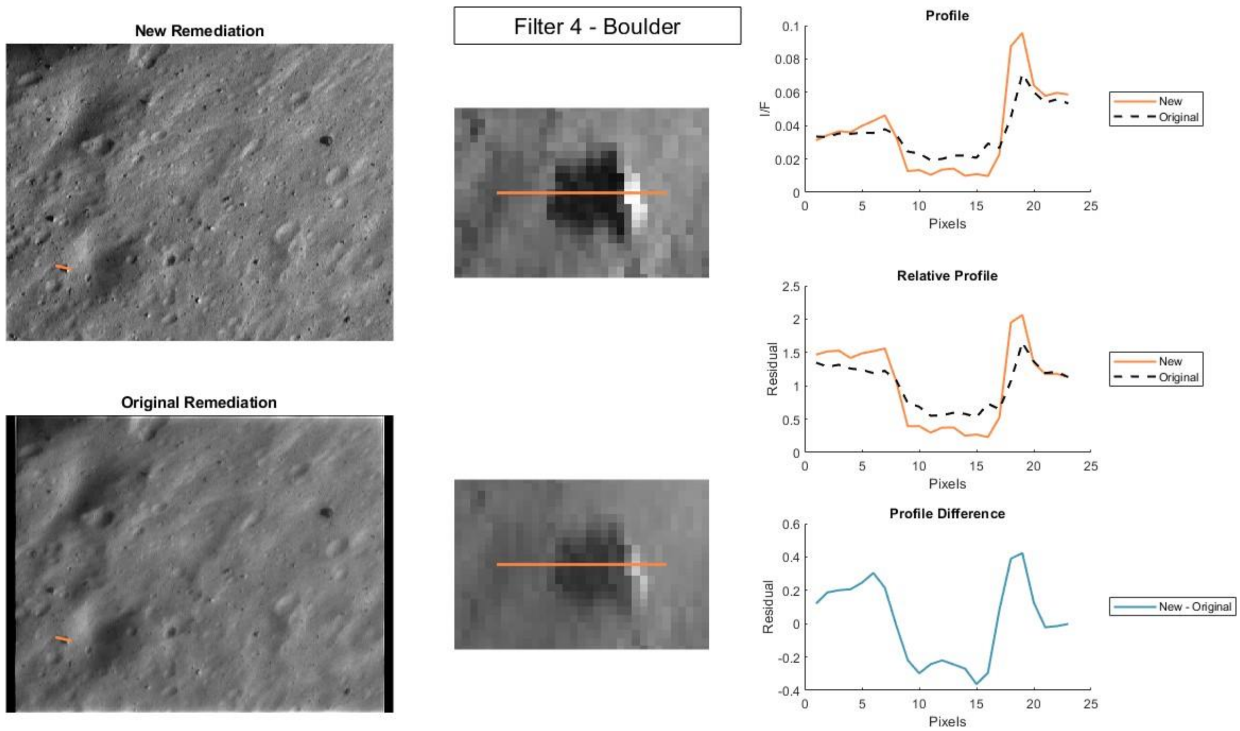

Figure 16: Profile analysis of a XX m boulder at 950 nm (m0155818916).

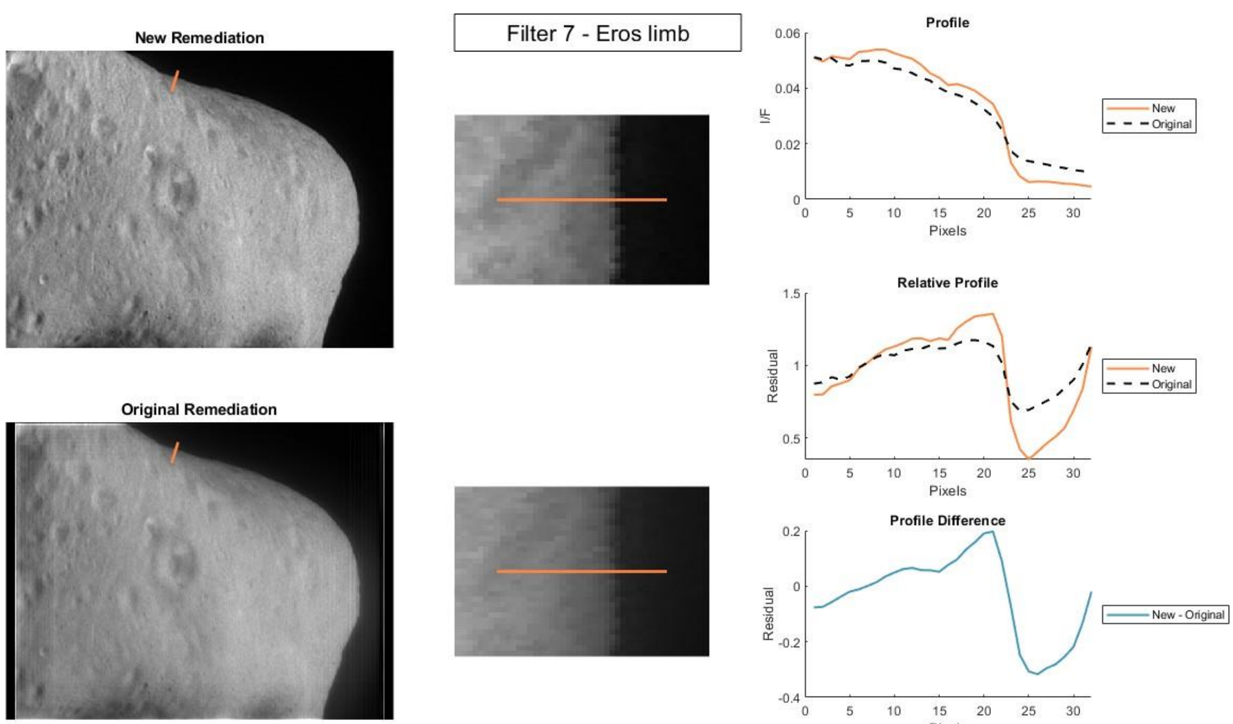

Figure 17: Profile analysis of the asteroid limb at 1050 nm (m0151057168).

4 Radiometric Correction

Blur remediation shifts a significant portion of the optical energy between pixels. Consequently, the radiometric (radiance or I/F) values are incorrect without further correction. We follow the strategy outlined in (Li et al., 2002) to apply an absolute radiometric calibration, wherein we assume that energy is conserved in the remediation process. That is, all energy measured in the original (degraded) images exists in the final (remediated) images, it has only been shifted between pixels. Therefore, we forced the sum of the energy in the region surrounding the asteroid in a remediated image to match that in its corresponding degraded image. This is only accurate when we perform it on a whole disk image (Figure 18), where all measured energy is captured within the MSI field of view.

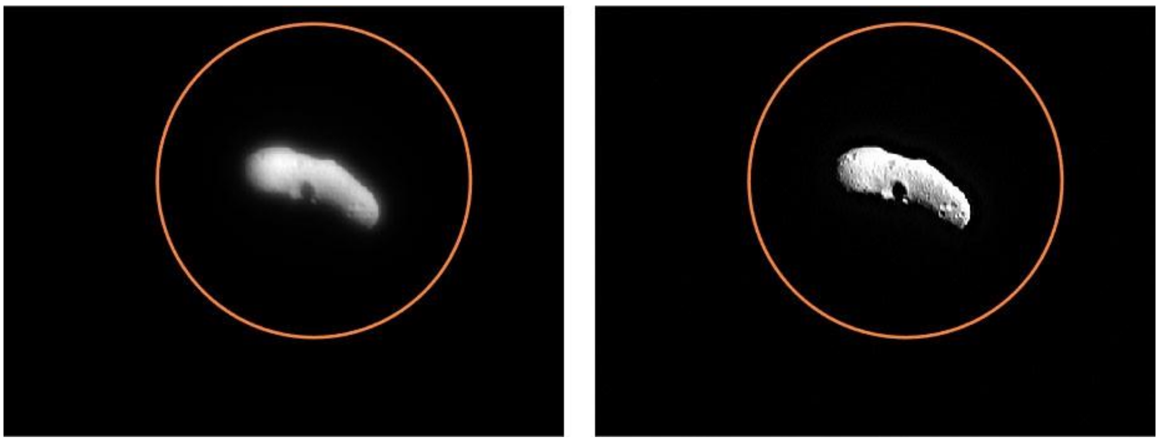

Figure 18: Degraded whole disk images (left) provide a radiometric normalization for recovered images (right) by summing the energy surrounding the asteroid (indicated by orange circle). The example shown was acquired with filter 4 (m0125680533).

Because the degraded images have signal past the asteroid limb (e.g., the glow and halo discussed in Section 2.7), we summed the energy well past the limb so that any blurred energy was captured in the sum. We tested summing the entire image versus summing a 150 pixel radius circle around Eros and found the differences to be <0.02% for all filters. We repeated this calculation for whole disk images acquired by all eight filters on 11 February and 12 February, 2000 (312 images total) and calculated the median radiometric correction for each filter. The number of images, per filter, and median radiometric correction are listed in Table 3. These values were calculated for and applied to the data described in this paper. Unfortunately, if a user applies their own remediation with the published code (Section 5), using customized PSF and noise term values, the radiometric correction parameters in Table 3 will be theoretically invalid. Though small changes in the remediation parameters will have a small effect on the radiometric correction, users should nonetheless take caution and consider calculating new radiometric correction factors by reproducing the radiometric analysis described here for differently deblurred data.

In any image where energy (i.e. Eros) is at the edge of the field of view, some of it will have been blurred off the detector. That energy is lost in the measurement and cannot be recovered. However, the surface that is just outside the field of view will partially blur onto the detector. To first order, these effects cancel each other out and do not require additional radiometric correction. This is not valid in edge cases where an extremely bright or dark scene is present at the edge of the field of view (e.g., an image where the asteroid limb is exactly at the edge of the image). However, we assume that these cases are sufficiently rare that we take no additional steps to accommodate them.

Table 3: Radiometric corrections for each filter

Filter (wavelength, nm)	**Number of images**	**Radiometric correction**
1 (550)	43	32.49
2 (450)	43	69.66
3 (760)	43	21.03
4 (950)	42	14.54
5 (900)	43	15.77
6 (1000)	43	18.26
7 (1050)	42	17.61
0 (pan)	12	24.68

We verified the relative (filter-to-filter) radiometric calibration by calculating a spectrum of Eros using the same whole disk images and comparing to published spectra (Murchie et al., 2002a; Murchie, 1996). We normalized the data at 550 nm to eliminate the absolute radiometric component. The difference between our calibration and the published spectra is within the MSI radiometric uncertainty (5%) determined by Murchie et al. (2002b, 1999) and within the difference between the published spectra.

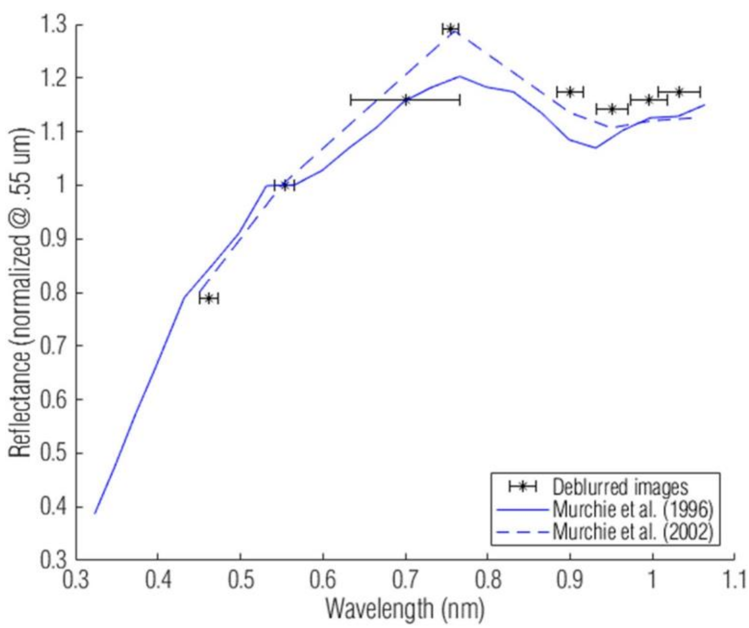

Figure 19: Comparison of relative radiometric calibration of the new remediation (black asterisks) with published spectra of Eros (blue lines). Horizontal error bars indicate the width of each MSI filter.

5 CODE AVAILABILITY AND CONCLUSIONS

We have updated the blur remediation method first published by Li et al. (2002) to utilize an asymmetric model of the MSI optics after hydrazine contamination. This new model, which we functionally define as the sum of three Gaussians, allows for recovery of additional spatial content from the degraded images. We add tapered symmetric padding to the FFT-based deconvolution to eliminate the FFT artifacts that were present along the edges of images with the original remediation. The changes increase the usable pixels in the images by 21-39%. We demonstrated this improvement both visually and with the contrast examples given in Section 3.3. However, an objective measure of ‘improvement’ is illusive and depends strongly on the desired application of the images.

We have applied the new correction to all MSI images acquired during 2000 and 2001 that are currently available in the PDS SBN (https://sbn.psi.edu/pds/resource/near/msiinst.html). We will archive the newly corrected images at the PDS Imaging Node. As noted in Section 2.3, the images are not compressed back to their native pixel format (as the raw and original remediation data are); they are left at the physically meaningful aspect ratio (412×537).

As demonstrated in the variety of examples provided in this manuscript, the choice of PSF and noise terms is inherently arbitrary and sensitive. Although the remediation we present here (and archived with the PDS) was performed with terms that we believed produced the best trade-off between sharpness and noise, these choices may not apply to all images or applications. Color analyses are typically very sensitive to pixel-level noise (DellaGiustina et al., 2020; Murchie et al., 2002a; Tatsumi et al., 2021), which is amplified in color ratios. As such, a color analysis may wish to apply a different correction level to the images. For example, in color analyses that are beyond the scope of this manuscript, we have found that color ratios (using overlapping images from different filters) require noise removal techniques (e.g., low pass filtering and Gaussian blurring) to maintain spatially coherent structure. This filtering essentially removes much of the sharpness recovered in this work.

Our analyses found that using the newly remediated images is an improvement because it allows for underlying, single-filter basemaps to have improved contrast (Section 3.3) and updated radiometric correction (Section 4). However, to provide the most utility from this remediation, we are also publishing the code used to apply the remediation. That code is seeded with the PSF and noise term values given in Table 2, but those values can be adjusted as needed for individual scientific analyses. The code is written in MATLAB and is available at https://doi.org/10.6084/m9.figshare.21842979.v1.

6 ACKNOWLEDGMENTS

This work comes two decades after the end of the NEAR mission, the success of which was due to a large number of individuals in the operational and scientific teams. Their efforts provided the exceptional dataset we attempted to improve. The work here builds directly off the original remediation developed by the MSI team, specifically Han Li and Mark Robinson, during NEAR operations. We also thank Beth Clark for her insight and reviewing the manuscript.

The original image data used in this work are archived in the Planetary Data System Small Bodies Node at https://sbn.psi.edu/pds/resource/near/msiinst.html. This work was supported by NASA under Contract NNH18ZDA001N-PDART issued through the Planetary Data, Archiving, Restoration, and Tools program.

7 REFERENCES

Acton, C., Bachman, N., Semenov, B., Wright, E., 2018. A look towards the future in the handling of space science mission geometry. P&SS 150, 9–12. https://doi.org/10.1016/j.pss.2017.02.013

Buczkowski, D.L., Barnouin-Jha, O.S., Prockter, L.M., 2008. 433 Eros lineaments: Global mapping and analysis. Icarus 193, 39–52. https://doi.org/10.1016/j.icarus.2007.06.028

Bussey, D.B.J., Robinson, M.S., Edwards, K., Thomas, P.C., Joseph, J., Murchie, S., Veverka, J., Harch, A.P., 2002. 433 Eros Global Basemap from NEAR Shoemaker MSI Images. Icarus 155, 38–50. https://doi.org/10.1006/icar.2001.6771

Cheng, A.F., Izenberg, N., Chapman, C.R., Zuber, M.T., 2002. Ponded deposits on asteroid 433 Eros. Meteoritics and Planetary Science 37, 1095–1105. https://doi.org/10.1111/j.1945-5100.2002.tb00880.x

Cheng, A.F., Santo, A.G., Heeres, K.J., Landshof, J.A., Farquhar, R.W., Gold, R.E., Lee, S.C., 1997. Near-Earth Asteroid Rendezvous: Mission overview. JGRE 102, 23695–23708. https://doi.org/10.1029/96JE03364

DellaGiustina, D.N., Burke, K.N., Walsh, K.J., Smith, P.H., Golish, D.R., Bierhaus, E.B., Ballouz, R.-L., Becker, T.L., Campins, H., Tatsumi, E., Yumoto, K., Sugita, S., Deshapriya, J.D.P., Cloutis, E.A., Clark, B.E., Hendrix, A.R., Sen, A., Al Asad, M.M., Daly, M.G., Applin, D.M., Avdellidou, C., Barucci, M.A., Becker, K.J., Bennett, C.A., Bottke, W.F., Brodbeck, J.I., Connolly, H.C., Delbo, M., de Leon, J., Drouet d'Aubigny, C.Y., Edmundson, K.L., Fornasier, S., Hamilton, V.E., Hasselmann, P.H., Hergenrother, C.W., Howell, E.S., Jawin, E.R., Kaplan, H.H., Le Corre, L., Lim, L.F., Li, J.Y., Michel, P., Molaro, J.L., Nolan, M.C., Nolau, J., Pajola, M., Parkinson, A., Popescu, M., Porter, N.A., Rizk, B., Rizos, J.L., Ryan, A.J., Rozitis, B., Shultz, N.K., Simon, A.A., Trang, D., Van Auken, R.B., Wolner, C.W. V., Lauretta, D.S., 2020. Variations in color and reflectance on the surface of asteroid (101955) Bennu. Science 370, eabc3660. https://doi.org/10.1126/science.abc3660

Dhawan, A.P., Rangayyan, R.M., Gordon, R., 1985. Image restoration by Wiener deconvolution in limited-view computed tomography. Applied Optics 24, 4013. https://doi.org/10.1364/AO.24.004013

Dombard, A.J., Barnouin, O.S., Prockter, L.M., Thomas, P.C., 2010. Boulders and ponds on the Asteroid 433 Eros. Icarus 210, 713–721. https://doi.org/10.1016/j.icarus.2010.07.006

Golish, D.R., Drouet d'Aubigny, C., Rizk, B., DellaGiustina, D.N., Smith, P.H., Becker, K., Shultz, N., Stone, T., Barker, M.K., Mazarico, E., Tatsumi, E., Gaskell, R.W., Harrison, L., Merrill, C., Fellows, C., Williams, B., O'Dougherty, S., Whiteley, M., Hancock, J., Clark, B.E., Hergenrother, C.W., Lauretta, D.S., 2020. Ground and In-Flight Calibration of the OSIRIS-REx Camera Suite. SSRv 216, 12. https://doi.org/10.1007/s11214-019-0626-6

Hawkins, S.E., 1998. The NEAR multispectral imager. Johns Hopkins APL Technical Digest (Applied Physics Laboratory) 19, 107–114.

Hawkins, S.E., Darlington, E.H., Murchie, S.L., Peacock, K., Harris, T.J., Hersman, C.B., Elko, M.J., Prendergast, D.T., Ballard, B.W., Gold, R.E., Veverka, J., Robinson, M.S., 1997. Multi-Spectral Imager on the Near Earth Asteroid Rendezvous mission. SSRv 82, 31–100. https://doi.org/10.1023/A:1005099211710

Izenberg, N.R., Murchie, S.L., Bell, J.F., McFadden, L.A., Wellnitz, D.D., Clark, B.E., Gaffey, M.J., 2003. Spectral properties and geologic processes on Eros from combined NEAR NIS and MSI data sets. Meteoritics and Planetary Science 38, 1053–1077. https://doi.org/10.1111/j.1945-5100.2003.tb00298.x

Janesick, J.R., 2001. Scientific Charge-Coupled Devices. SPIE, 1000 20th Street, Bellingham, WA 98227-0010 USA. https://doi.org/10.1117/3.374903

Li, H., Robinson, M.S., Murchie, S., 2002. Preliminary Remediation of Scattered Light in NEAR MSI Images. Icarus 155, 244–252. https://doi.org/10.1006/icar.2001.6745

Li, J., A'Hearn, M.F., McFadden, L.A., 2004. Photometric analysis of Eros from NEAR data. Icarus 172, 415–431. https://doi.org/10.1016/j.icarus.2004.07.024

Murchie, S., Robinson, M., Clark, B., Li, H., Thomas, P., Joseph, J., Bussey, B., Domingue, D., Veverka, J., Izenberg, N., Chapman, C., 2002a. Color Variations on Eros from NEAR Multispectral Imaging. Icarus 155, 145–168. https://doi.org/10.1006/icar.2001.6756

Murchie, S., Robinson, M., Domingue, D., Li, H., Prockter, L., Hawkins, S.E., Owen, W., Clark, B., Izenberg, N., 2002b. Inflight Calibration of the NEAR Multispectral Imager II. Results from Eros Approach and Orbit. Icarus 155, 229–243. https://doi.org/10.1006/icar.2001.6746

Murchie, S., Robinson, M., Hawkins, S.E., Harch, A., Helfenstein, P., Thomas, P., Peacock, K., Owen, W., Heyler, G., Murphy, P., Darlington, E.H., Keeney, A., Gold, R., Clark, B., Izenberg, N., Bell, J.F., Merline, W., Veverka, J., 1999. Inflight Calibration of the NEAR Multispectral Imager. Icarus 140, 66–91. https://doi.org/10.1006/icar.1999.6118

Murchie, S.L., 1996. Spectral properties and rotational spectral heterogeneity of 433 Eros. JGRE 101, 2201–2214. https://doi.org/10.1029/95JE03438

Riner, M.A., Robinson, M.S., Eckart, J.M., Desch, S.J., 2008. Global survey of color variations on 433 Eros: Implications for regolith processes and asteroid environments. Icarus 198, 67–76. https://doi.org/10.1016/j.icarus.2008.07.007

Robinson, M.S., Thomas, P.C., Veverka, J., Murchie, S.L., Wilcox, B.B., 2002. Invited Review The geology of 433 Eros, Meteoritics & Planetary Science.

Sierks, H., Keller, H.U., Jaumann, R., Michalik, H., Behnke, T., Bubenhagen, F., Büttner, I., Carsenty, U., Christensen, U., Enge, R., Fiethe, B., Gutiérrez Marqués, P., Hartwig, H., Krüger, H., Kühne, W., Maue, T., Mottola, S., Nathues, A., Reiche, K.-U., Richards, M.L., Roatsch, T., Schröder, S.E., Szemerey, I., Tschentscher, M., 2011. The Dawn Framing Camera. SSRv 163, 263–327. https://doi.org/10.1007/s11214-011-9745-4

Tatsumi, E., Sakatani, N., Riu, L., Matsuoka, M., Honda, R., Morota, T., Kameda, S., Nakamura, T., Zolensky, M., Brunetto, R., Hiroi, T., Sasaki, S., Watanabe, S., Tanaka, S., Takita, J., Pilorget, C., de León, J., Popescu, M., Rizos, J.L., Licandro, J., Palomba, E., Domingue, D., Vilas, F., Campins, H., Cho, Y., Yoshioka, K., Sawada, H., Yokota, Y., Hayakawa, M., Yamada, M., Kouyama, T., Suzuki, H., Honda, C., Ogawa, K., Kitazato, K., Hirata, Naru, Hirata, Naoyuki, Tsuda, Y., Yoshikawa, M., Saiki, T., Terui, F., Nakazawa, S., Takei, Y., Takeuchi, H., Yamamoto, Y., Okada, T., Shimaki, Y., Shirai, K., Sugita, S., 2021. Spectrally blue hydrated parent body of asteroid (162173) Ryugu. NatCo 12. https://doi.org/10.1038/s41467-021-26071-8

Thomas, P.C., Joseph, J., Carcich, B., Veverka, J., Clark, B.E., Bell, J.F., Byrd, A.W., Chomko, R., Robinson, M., Murchie, S., Prockter, L., Cheng, A., Izenberg, N., Malin, M., Chapman, C., McFadden, L.A., Kirk, R., Gaffey, M., Lucey, P.G., 2002. Eros: Shape, topography, and slope processes. Icarus 155, 18–37. https://doi.org/10.1006/icar.2001.6755

Thomas, P.C., Robinson, M.S., 2005. Seismic resurfacing by a single impact on the asteroid 433 Eros. Nature 436, 366–369. https://doi.org/10.1038/nature03855

Veverka, J., Robinson, M., Thomas, P., Murchie, S., Bell, J.F., Izenberg, N., Chapman, C., Harch, A., Bell, M., Carcich, B., Cheng, A., Clark, B., Domingue, D., Dunham, D., Farquhar, R., Gaffey, M.J., Hawkins, E., Joseph, J., Kirk, R., Li, H., Lucey, P., Malin, M., Martin, P., McFadden, L., Merline, W.J., Miller, J.K., Owen, J., Peterson, C., Prockter, L., Warren, J., Wellnitz, D., Williams, B.G., Yeomans, D.K., 2000. NEAR at Eros: Imaging and spectral results. Science 289, 2088–2097. https://doi.org/10.1126/science.289.5487.2088

Zuber, M.T., Smith, D.E., Cheng, A.F., Garvin, J.B., Aharonson, O., Cole, T.D., Dunn, P.J., Guo, Y., Lemoine, F.G., Neumann, G.A., Rowlands, D.D., Torrence, M.H., 2000. The shape of 433 Eros from the NEAR-Shoemaker Laser Rangefinder. Science 289, 2097–2101. https://doi.org/10.1126/science.289.5487.2097